CRM Master Research Projects

Modelling of Non-linear Viscoelastic Tissues with Bar Elements

Author: Nina Asadipour

Advisor: José Javier Muñoz Romero

MASTER'S DEGREE THESIS

Master of Science in Advanced Mathematics and Mathematical Engineering

Title: Modelling of non-linear viscoelastic tissues with bar elements

Author: Nina Asadipour

Advisor: Jose Javier Muñoz Romero

Department: Matemàtica Aplicada III

Academic year:2011-2012

Facultat de Matemàtiques i Estadística

UNIVERSITAT POLITÈCNICA DE CATALUNYA

Universitat Politècnica de Catalunya

Facultat de Matemàtiques i Estadística

Thesis submitted for the Master of Science in
Advanced Mathematics and Mathematical Engineering

Modelling of non-linear viscoelastic tissues with bar elements

Nina Asadipour

Director:Jose Javier Muñoz Romero

Departament de Matemàtica Aplicada III

Abstract

In this work we develop a viscoelastic bar element that can handle multiple rheological laws with non-linear elastic and non-linear viscous material models. The bar element is built by joining in series an elastic and viscous bar, constraining the middle node position to the bar axis with a reduction method, and statically condensing the internal degrees of freedom. We apply the methodology to the modelling of reversible softening with stiffness recovery both in 2D and 3D, a phenomenology also experimentally observed during stretching cycles on epithelial lung cell monolayers.

Acknowledgements

First and foremost I offer my sincerest gratitude to my supervisor, Dr josé muñoz, who has supported me thoughout my thesis with his patience and without whose knowledge and assistance this study would not have been successful.

I am most indebted to Philippe Alexandre Pouille for helping me learn the Bio part and allowing me to use Confocal microscopy.

I would like to thank my family members, especially my sister, Moona Asadipour , and her Husband, Tom Creemers for supporting and encouraging me to pursue this degree.

I wish to thank my best friend, Mohammad Kouhi, for helping me get through the difficult times, and for all the emotional support.

This work was financially supported by the Center Reseach Mathematic institue.

This thesis is in collaboration with two biology labs at Parc Cientific de Barcelona (main researchers, Enrique Martin Blanco and Xavier Trepat), which are interested in the mechanical characterisation of the embryonic cells, and looking at testing the relevant parameters that govern cell active deformations. This relation was initiated more than one year ago by the contribution of a post-doctoral student of the Msc Thesis supervisor, José muñoz.

Contents

List of Figures

Chapter 1

Introduction

1.1 Background

Well before the discovery of the polymeric cytoskeleton in the 1950s [1], a controversy erupted as to whether the physical nature of the cell interior (or protosplasm) was fibrous, granular, or alveolar. At the core of this controversy was the observation that shear altered the mechanical properties of the cell. Andrews (1897) and Mathews and Whitcher (1903) were the first to report that mechanical agitation caused cell viscosity to increase [2, 3]. Such observations stood in contrast with those of Chambers (1917) who noted that churning a fertilized sand-dollar egg with a micro-needle resulted in reversible disappearance of the aster and in a reversible liquefaction of the protoplasm [4]. Almost a decade later, Mast (1926) proposed as the driving mechanism for amoeba migration a similar solid to liquid transition between a solid-like cell cortex (the paslmagel) and a liquid-like cell interior (the plasmasol) [5]. By observing granules suspended in the plasmagel, he was astonished to find that, if a given granule in the plasmagel is carefully observed, it is found that, while it may move continuously for an apparently indefinite period of time, it does not progress beyond the boundaries of a very small area. From such observations he concluded that the structure of the cell was alveolar rather than fibrous, with each granule trapped inside an alveolus. This conclusion was similar to that obtained by Butschli, who proposed in 1894 that the cells derived their physical properties from a foam-like structure [6].

A major milestone in the history of rheology was the introduction of thixotropy by Freundlich and co-workers in 1926 [7]. Their findings led several investigators to study whether thixotropy could apply not only to soft inert matter but also to soft living matter. As such, in 1928 Abramson proposed that the passage of leucocytes through narrow capillaries during inflammation was favored by the ability of the cells of the capillary wall to be fluidized by shear [8]. The first quantitative observations of shear fluidization were not provided until Angerer in 1936. Using a shaking device coupled to a centrifuge he was able to quantitatively measure a drop in the viscosity of the protoplasm of $20 - 60\%$

as a consequence of high frequency shear followed by a slow recovery towards baseline values [9].

Thus, the hallmarks of soft glassy matter including shear fluidization (thixotropy), crowding, and trapping of particles by their neighbors, had already been identified in the living cell-although not without substantial controversy-as long ago as the late part of the 19th and early part of the 20th centuries. But with the subsequent discovery of the polymeric cytoskeleton, the emergence of polymer physics, and modern theories of semiflexible networks that stiffen with strain instead of being fluidized, these early seminal observations were all but forgotten.

1.1.1 Cell fluidization

All living things, despite their profound diversity, share a common architectural building block: the cell. Cells are the basic functional units of life, yet are themselves comprised of numerous components with distinct mechanical characteristics. To perform their various functions, cells undergo or control a host of intra- and extracellular events, many of which involve mechanical phenomena or that may be guided by the forces experienced by the cell. The subject of cell mechanics encompasses a wide range of essential cellular processes, ranging from macroscopic events like the maintenance of cell shape, cell motility, adhesion, and deformation to microscopic events such as how cells sense mechanical signals and transduce them into a cascade of biochemical signals ultimately leading to a host of biological responses [10].

The field of cell mechanics recently has undergone rapid development with particular attention to the rheology of the cytoskeleton and the reconstituted gels of some of the major cytoskeletal components actin filaments, intermediate filaments, microtubules, and their cross-linking proteins that collectively are responsible for the main structural properties and motilities of the cell. Another area of intense investigation is the mechanical interaction of the cell with its surroundings and how this interaction causes changes in cell morphology and biological signaling that ultimately lead to functional adaptation or pathological conditions.

Nowhere is the importance of biology in cell mechanics more evident than in the ability of the cell to sense and respond to externally applied forces. Many-perhaps all cells are able to sense when a physical force is applied to them. They respond through a variety of biological pathways that lead to such diverse consequences as changes in membrane channel activity, up or down regulation of gene expression, alterations in protein synthesis, or altered cell morphology.

The presence of viscous effects component in elastic materials may become non-negligible in many relevant applications in engineering and biomedicine. One of such prominent applications is the analysis of soft materials in biomechanics such as skin [19], developmental epithelia [20], or arteries [21], whose

viscous nature cannot be discounted. Laboratory experiments have also shown that not only may the elastic component become non-linear, but also the viscous effects may depend on the actual deformation or stress-state [22]. The modelling and handling of these non-linearities in a simple manner has motivated the present work.

Despite recent measurements on the mechanical properties of soft tissues during embryo development, there is currently no consensus on neither the solid and fluid nature of the material nor on the parameters that govern the observed deformations.

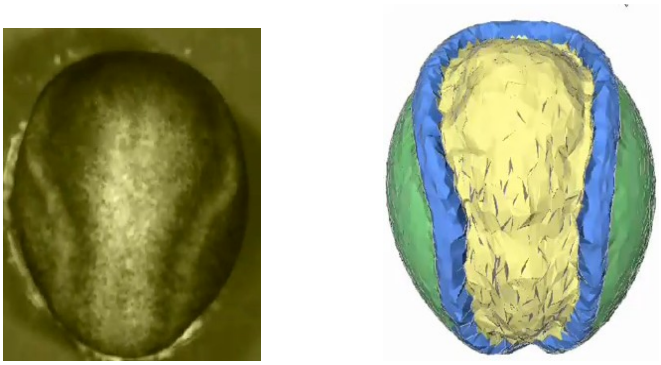

(a) (b)

Figure 1.1: Fluid model of cell by Chen et all (a) Experimental results and (b) Numerical 3D results

Do cells behave as fluids, or as solids?

Under physiologic loading conditions, many cell types undergo significant mechanical loads and deformations that have been implicated in regulating cellular signal transduction pathway [11]. Consequently, knowledge of cell mechanics is an important component of broader biomechanical studies in mammalian tissues. Structurally, cells are inhomogeneous materials, in that they are comprised of a nucleus, cytoplasm, cell membrane and multiple intracellular organelles. While the focous of this work is on model that idealize the cell as a solid or mixture continuum, it is noted that other approaches have developed stractural models of the cell, tensegrity [12, 13].

Within the continuum framework, models enable determination of mechanical properties such as elastic stiffness moduli, fluid viscoelasity and viscoelastic relaxation times. Continuum models can be grouped into two categories, roughly characterizied as *fluid models* and *solid models*. In the former case, the intracellular environment is idealized as a viscous or a viscoelastic fluid with some models accounting for cortical tension in the cell membrane or a cytoskeletal network of immersed viscoelastic fibers [14]. In the later category, the whole cell is idealized as an elastic, viscoelastic and has the capacity to store

strain energy at equilibrium [15].

Tipically, fluid models have been applied to cell mechanics in the circulatory system, such as neutrophils or lymphocytes, while solid models more accurately characterize mechanics of chondrocytes, fibroblasts and endothelial cells [16].

In the work done by Chen et all, a fluid model of the tissues and cells are investigated. They utilized a computational model to understand the forces that drive cell and tissue motions in contexts such as embryogenesis, regenerative medicine and cancer Metastasis. Two different level model consist of cell-level and tissue-level are considered in their research (Figure1.1). As a solid model, we can refer to the research carried out by Conte et all where a solid model of the cells are investigated. They have developed a 3D finite element method model of ventral furrow formation by decomposing the total deformation into two parts: an imposed active deformation, and an elastic passive deformation (Figure1.2).

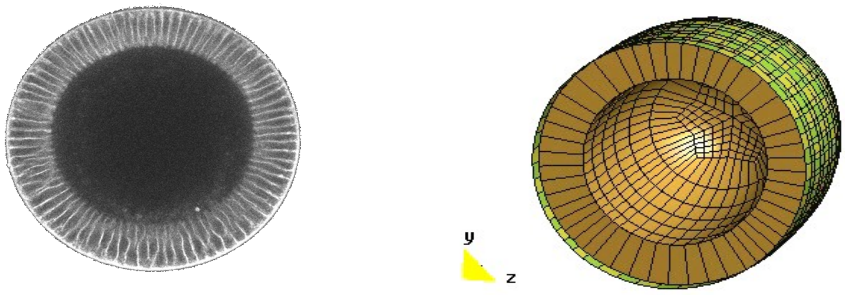

(a) (b)

Figure 1.2: Solid model of cell by Conte et all (a) Experimental results and (b) Numerical 3D results

1.1.2 Stretch in the living cell

With every beat of the heart, inflation of the lung or peristalsis of the gut, cell types of diverse function are subjected to substantial stretch. Stretch is a potent stimulus for growth, differentiation, migration, remodelling and gene expression [17, 18]. Soft materials such as tomato ketchup, shaving foam and tooth paste tend to fluidize when subjected to shear, as do granular materials including sugar in a bowl, coffee beans in a chute and even certain geophysical strata during an earthquake; each transforms from a solid-like to a fluid-like phase, stiffness falls, and the material flows. Underlying microscopic stress-bearing elements, or clusters of elements, interact with neighbours to form a network of force transmission, but how flow is initiated and the nature of energy barriers that must be overcome remain the subject of much current attention.
The response of a living cell to transient stretch would seem to be a different

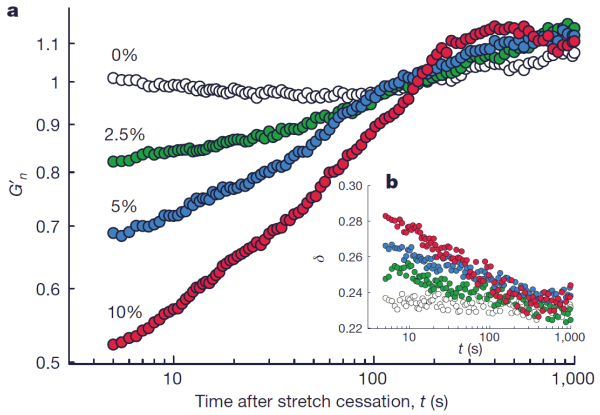

Figure 1.3: A single transient stretch drives fractional stiffness G'_n down and the phase angle δ up, indicating fluidization of the cytoskeleton. a, Evolution of G'_n of HASM cells after a single transient stretch of 0%, 2.5% (green), 5% (blue) and 10% (red). b, Evolution of the phase angle after stretch application.

matter altogether. Very early literature shows that in response to application of a physical force the cell acutely softens, but more recent literature uniformly emphasizes stiffening. Nevertheless, in 2007, Xavier Trepat and his group demonstrate that the living cell promptly fluidizes and then slowly re-solidifies much as do the inert systems. Moreover, underlying structural rearrangements on the nanometre scale promptly accelerate and then slowly relax [22]. A novel experimental system is developed by them in which they could model the viscoelastic behaviour of the living cells. They subject the adherent human airway smooth muscle (HASM) cell to a transient isotropic biaxial stretch-unstretch manoeuvre. They could then monitor, on the nanometre scale, cell mechanical properties, remodelling dynamics and their changes.

In that work, stiffness after stretch relative to stiffness of the same cell immediately before was denoted G'_n. As shown in 1.3 a, when no stretch was applied, this fractional stiffness did not change, but immediately after cessation of a single transient stretch G'_n promptly decreased and then slowly recovered. Immediately after stretch cessation, the phase angle $\delta = tan^{-1}(G''/G')$ promptly increased and then slowly recovered, where for a hookean solid $\delta = 0.5$ and for a newtonian fluid $\delta = \frac{\pi}{2}$. In the living cell $0.15 \leq \delta \leq 0.50$, thus placing the living cell closer to the solid-like state, and δ is virtually invariant with changes of frequency, thus setting cytoskeleton rheology within the paradigms of structural damping and scale-free dynamics.

In the current study, in order to obtain the mentioned characteristics of the living cells, a new numerical modelling is investigated based on the concept of non-linear viscoelastic materials in loading and unloading paterns.

1.1.3 Rheological models

The word viscoelastic is derived from the words "viscous" + "elastic"; a viscoelastic material exhibits both viscous and elastic behaviour a bit like a fluid and a bit like a solid. One can build up a model of linear viscoelasticity by considering combinations of the linear elastic spring and the linear viscous dash-pot. A non-linear theory can be developed by including non-linear springs and dash pots. These are known as **rheological models** or **mechanical models**.
The two fundamental rheological laws for the modelling of viscoelasticity are the Kelvin-Voigt and Maxwell models. The former is best suited for modelling creep (strain relaxation) in a stress controlled test, while the latter is able to reproduce stress relaxation in a displacement controlled test. The generalised Maxwell model is a combination of the two models, and gathers the advantages of both. It is therefore better suited for fitting general viscoelastic materials [25]. The characterization of the viscoelastic response of materials in one dimension has been well studied [23, 24]. Its extension to multiple dimensions and its finite element implementations in the linear regime where originally developed more than thirty years ago [26, 27]. However, when extending these formulations to finite elasticity, some internal variables and evolution laws must be hypothesised and numerically solved [29, 30, 31]. Such evolution laws may be written as a function of the principal stretches [28], or in materials with fibres, in terms of the preferred material directions [32]. In these formulations, the elastic and viscous stresses are numerically solved in a robust monolithic manner by using linear viscoelastic evolution laws. Although this procedure may be advantageous in a finite element context, it makes the resolution of problems with more complex non-linearities hihgly dependent on the rheological law at hand.

1.2 Motivation and scope of thesis

The aim of this work is to model soft tissues by employing a simplified system of visco-elastic bars. Such bars mimic the mechanical behaviour of the solid skeleton of the cell (cytoskeleton), which is composed by filaments of different width, mainly, from thicker to thinner: microtubules, intermediate filaments and actin filaments. The rods of the model are able to reproduce non-linear visco-elastic behaviour. The model will enable to test some of the postulated evolution laws for the active deformation of cells (stress-dependent growth) and for the strain-dependent elastic and viscous properties of the tissue.

Mathematically, the model must solve the non-linear equilibrium equations of the three-dimensional bar system of tetrahedra (triangles in 2D), subjected to some constraints such as contact and incompressibility. More specifically, we aim to reproduce the following two sources of non-linearities:

i) Material non linearity: The material model corresponds to a generalised Maxwell rheological law (a series of springs and dashpots, in parallel with a spring element), with non-linear viscoelastic properties.

ii) Geometrical non-linearities: the bars are able to undergo large deformations and displacements. The formulation is therefore able to describe the

stress-strain relation in arbitrary orientations of the bars, yielding a non-linear stress-strain description.

The rheological model developed here can show the linear or nonlinear behavior of the material through the specification of spring and dashpot. In order to model the non-linear rheological law, the work includes the development of a novel bar element that consists on the modelling of a series of bars, with the middle nodes aligned along the line joining the end nodes, The model imposes such material constraints using null-space projection and static condensation of the internal coordinates (position of the middle nodes).

1.3 Outline of this work

The rest of this work are as following: In Chapter 2 viscoelastic rheological models of tissues are presented containing the Maxwell model, Kelvin model and Generalized model. The Monolithic solution of the Maxwell model as well as the Maxwell element formulation are introduced in Section 2.1. In this Section, by developing a new representation of the bar element, the corresponding stiffness matrixes and elemental residuals are obtained based on the two methods of null-space projection and static condensation. Then, the linear and non-linear constitutive laws for elastic and viscous materials are studied. In Section 2.2 and 2.3, the Kelvin model and generalized Maxwell model are presented. The process of stress recovery of the proposed model is given in Section 2.4. In chapter 3, the numerical results related to one dimention, two dimention and three dimention bar elements are shown to test the capability of the present method. The summarized conclusions and the future work are discussed in chapter 4.

Chapter 2

Viscoelastic rheological models

2.1 The Maxwell model

In this section first the Monolithic solution of the Maxwell model as well as the elemental formulation are introduced. Then, by developing a new representation of the bar element, the corresponding stiffness matrixes and elemental residuals are obtained based on the two methods of null-space projection and static condensation. Finally, the linear and non-linear constitutive laws for elastic and viscous materials are studied.

2.1.1 Monolithic solution

Although the methodology explained in this Section is easily extensible to multi-dimensional analysis, we will focus on one dimensional rheological laws in order to ease the exposition and to relate the results to the subsequent bar element. We aim to deal with general elastic and viscous laws expressible in the forms:

$$\begin{matrix} \sigma^e(\varepsilon^e) \\ \sigma^v(\dot{\varepsilon}^v) \end{matrix} \tag{2.1}$$

where σ^e and σ^v are the elastic and viscous stresses, ε^e and ε^v the elastic and viscous strains and the superposed dot indicates time derivative. In the linear case, relations (2.1) are expressed as,

$$\begin{matrix} \sigma^e = k\varepsilon^e \\ \sigma^v = \eta\dot{\varepsilon}^v \end{matrix} \tag{2.2}$$

with k and η the material stiffness and viscosity, respectively. In a Maxwell element we have that $\sigma^e = \sigma^v = \sigma$, while the strains must satisfy the following

kinematic constraint:

$$\dot{\varepsilon} = \dot{\varepsilon}^e + \dot{\varepsilon}^v \tag{2.3}$$

with ε the total strain. Algorithms to numerically solve the equilibrium equations with this rheological law were originally proposed in [36, 37, 26]. In these references, equations (2.2) and (2.3) are combined in order to isolate the stress rate as follows,

$$\dot{\sigma} = k\left(\dot{\varepsilon} - \frac{\sigma}{\eta}\right)$$

which after time-discretisation, and setting $\sigma_{n+\theta} = (1-\theta)\sigma_n + \theta\sigma_{n+1}$ and $\Delta(\bullet))(\bullet)_{n+1} - (\bullet)_n$, allows us to express σ_{n+1} as,

$$\sigma_{n+1} = \left(1 + \frac{k\theta\Delta t}{\eta}\right)^{-1}\left(k\Delta\varepsilon + \left(1 + \frac{k\Delta t(\theta-1)}{\eta}\right)\sigma_n\right)$$

By inserting this relation into the equilibrium equations, the current displacements u_{n+1} may be obtained. The extension of such algorithm to multidimensional strain based viscoelasticity is straightforward. However, such procedure cannot be applied to general non-linear elastic and viscous laws like those in equation (2.1), or to analyses with large strains and displacements. In addition, bearing in mind that we aim to model viscoelastic behaviour of biological tissues formed by a network of unidimensional filaments, we propose an alternative methodology in this Section which accounts in a simple manner for material and geometrical non-linearities.

2.1.2 Maxwell element formulation

Bar kinematics and rheological splitting

The configuration of a bar element is defined by the positions of the two end points. At the initial (stress-free) and current configurations, they are respectively given by the couples $(\boldsymbol{X}_1, \boldsymbol{X}_2)$ and $(\boldsymbol{x}_1, \boldsymbol{x}_2)$.

The key idea consists in splitting the elastic and viscous components of a viscoelastic bar in a series of two distinct elements, in the same manner as it is done in equation (2.3). More specifically, the whole viscoelastic element, that joints nodes $\boldsymbol{x}_1$ and $\boldsymbol{x}_2$, has an additional intermediate node $\boldsymbol{x}_3$ that determines the elastic component (between nodes $\boldsymbol{x}_1$ and $\boldsymbol{x}_3$), and the viscous component (between nodes $\boldsymbol{x}_3$ and $\boldsymbol{x}_2$) (see Figure 2.1a). The elastic and viscous elements are allowed to have any general constitutive law.

As shown in Figure 2.1b, node $\boldsymbol{x}_3$ is constrained to move along the line joining nodes 1 and 2, and its position is thus determined by an internal variable λ as follows:

$$\boldsymbol{x}_3 = \boldsymbol{x}_1 + \lambda(\boldsymbol{x}_2 - \boldsymbol{x}_1)$$

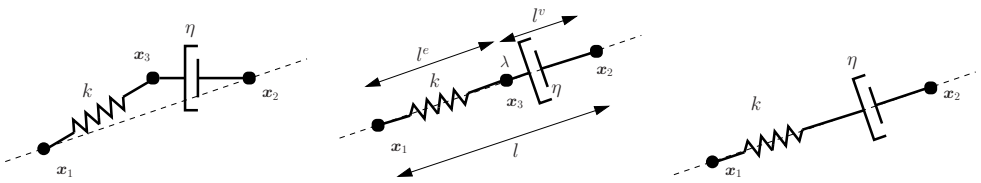

(a) (b) (c)

Figure 2.1: Representation of construction process of Maxwell element:(a) initial 2 elements, (b) constrained 2 elements where node 3 is enforced to move along line between nodes 1 and 2, and (c) final element after static condensation of internal dof λ.

or equivalently

$$\boldsymbol{\phi} := \boldsymbol{x}_3 - \lambda(\boldsymbol{x}_2 - \boldsymbol{x}_1) = \mathbf{0}. \tag{2.4}$$

The total initial (stress-free) and total current lengths of the bar are obtained as $L = \|\boldsymbol{X}_2 - \boldsymbol{X}_1\|$ and $l = \|\boldsymbol{x}_2 - \boldsymbol{x}_1\|$, respectively, while the elastic and viscous lengths of the bar will be denoted by $l^e = \|\boldsymbol{x}_1 - \boldsymbol{x}_3\|$ and $l^v = \|\boldsymbol{x}_2 - \boldsymbol{x}_3\|$. In agreement with the rheological splitting, the scalar elastic and viscous strains are defined by,

$$\varepsilon^e = \frac{l^e - L^e}{L} \quad , \quad \varepsilon^v = \frac{l^v - L^v}{L}. \tag{2.5}$$

As it can be verified, these definition satisfy the relation $\varepsilon = \varepsilon^e + \varepsilon^v$, with $\varepsilon = (l - L)/L$. We also point out that these strain measures are evaluated along the arbitrary bar direction, and also that the relation between the length measures l^e and l^v, and the nodal positions $\boldsymbol{x}_i$ is non-linear. Therefore, the strain measures correspond to non-linear co-rotated strains which can handle large bar displacements and rotations. Furthermore, since the value of l remains unchanged after applying a rigid body motion, the strain measures employed are objective.

We will next deduce a two-noded bar element with viscoelastic properties which in the linear case (no large rotations) is equivalent to the monolithic rheological model described in Section 2.1.1. The advantage of such an element is that it can handle any elastic and viscous constitutive laws, and can be employed in analyses with large deformations and displacements. The process consists in the following two basic steps: (i) the imposition of the kinematic constraint on node $\boldsymbol{x}_3$ by resorting to the null-space method, and (ii) the static condensation of the internal variable λ. These steps will be described in detail next.

2.1.3 Null-space projection

We will assume that the global equilibrium of the elastic and viscous part of a viscoelastic bar may constructed by assembling the following two general nodal residuals, denoted by $\hat{\boldsymbol{g}}^e$ and $\hat{\boldsymbol{g}}^v$, respectively:

$$\hat{\boldsymbol{g}}^e = \left\{ \begin{array}{c} \hat{\boldsymbol{g}}^e_1 \\ \hat{\boldsymbol{g}}^e_3 \end{array} \right\} \quad , \quad \hat{\boldsymbol{g}}^v = \left\{ \begin{array}{c} \hat{\boldsymbol{g}}^v_3 \\ \hat{\boldsymbol{g}}^v_2 \end{array} \right\}, \tag{2.6}$$

where the subscripts denote the node to which each component is associated. After assembling, the global residual $\hat{\boldsymbol{g}}$ and corresponding Jacobian $\hat{\mathbf{K}}$ are obtained,

$$\hat{\boldsymbol{g}} = \left\{ \begin{array}{c} \boldsymbol{g}^e_1 \\ \boldsymbol{g}^e_3 + \boldsymbol{g}^v_3 \\ \boldsymbol{g}^v_2 \end{array} \right\} = \left\{ \begin{array}{c} \hat{\boldsymbol{g}}_1 \\ \hat{\boldsymbol{g}}_3 \\ \hat{\boldsymbol{g}}_2 \end{array} \right\}, \tag{2.7}$$

$$\hat{\mathbf{K}} = \left[\begin{array}{ccc} \mathbf{K}^e_{11} & \mathbf{K}^e_{13} & \mathbf{0} \\ \mathbf{K}^e_{31} & \mathbf{K}^e_{33} + \mathbf{K}^v_{33} & \mathbf{K}^v_{32} \\ \mathbf{0} & \mathbf{K}^v_{23} & \mathbf{K}^v_{22} \end{array} \right] = \left[\begin{array}{ccc} \hat{\mathbf{K}}_{11} & \hat{\mathbf{K}}_{13} & \hat{\mathbf{K}}_{12} \\ \hat{\mathbf{K}}_{31} & \hat{\mathbf{K}}_{33} & \hat{\mathbf{K}}_{32} \\ \hat{\mathbf{K}}_{32} & \hat{\mathbf{K}}_{23} & \hat{\mathbf{K}}_{22} \end{array} \right], \tag{2.8}$$

which are conjugate to the virtual displacement vector $\{\delta\boldsymbol{x}_1^T, \delta\boldsymbol{x}_3^T,\ \delta\boldsymbol{x}_2^T\}$. The total work (elastic and dissipated in the viscous element) is then expressed as:

$$\mathcal{W} = \{\delta\boldsymbol{x}_1^T\ \delta\boldsymbol{x}_3^T\ \delta\boldsymbol{x}_2^T\}\hat{\boldsymbol{g}}. \tag{2.9}$$

On the other hand, the kinematic constraint in equation (2.4) induces the following relation between the virtual counterparts:

$$\delta\boldsymbol{x}_3 = (1-\lambda)\delta\boldsymbol{x}_1 + (\boldsymbol{x}_2 - \boldsymbol{x}_1)\delta\lambda + \lambda\delta\boldsymbol{x}_2. \tag{2.10}$$

This equation allows us to write the following relation between the unconstrained dof $\delta\{\boldsymbol{x}_1^T\ \lambda\ \boldsymbol{x}_2^T\}$ and the constrained dof $\delta\{\boldsymbol{x}_1^T\ \boldsymbol{x}_3^T\ \boldsymbol{x}_2^T\}$:

$$\delta \left\{ \begin{array}{c} \boldsymbol{x}_1 \\ \boldsymbol{x}_3 \\ \boldsymbol{x}_2 \end{array} \right\} = \left[\begin{array}{ccc} \mathbf{I} & \mathbf{0} & \mathbf{0} \\ (1-\lambda)\mathbf{I} & \boldsymbol{x}_2 - \boldsymbol{x}_1 & \lambda\mathbf{I} \\ \mathbf{0} & \mathbf{0} & \mathbf{I} \end{array} \right] \delta \left\{ \begin{array}{c} \boldsymbol{x}_1 \\ \lambda \\ \boldsymbol{x}_2 \end{array} \right\} = \mathbf{N}\delta \left\{ \begin{array}{c} \boldsymbol{x}_1 \\ \lambda \\ \boldsymbol{x}_2 \end{array} \right\}.$$

The total virtual work in (2.9) may be now re-expressed as,

$$\delta\mathcal{W} = \left\{\delta\boldsymbol{x}_1^T\ \delta\lambda\ \delta\boldsymbol{x}_2^T\right\}\mathbf{N}^T\hat{\boldsymbol{g}} = \left\{\delta\boldsymbol{x}_1^T\ \delta\lambda\ \delta\boldsymbol{x}_2^T\right\}\tilde{\boldsymbol{g}},$$

where matrix $\mathbf{N}$ *projects* the residual $\hat{\boldsymbol{g}}$ onto the new residual $\tilde{\boldsymbol{g}} := \mathbf{N}^T\hat{\boldsymbol{g}}$ which is conjugate to a reduced set of (unconstrained) variables, ($\delta\boldsymbol{x}_1$, $\delta\lambda$, $\delta\boldsymbol{x}_2$). In fact, the first and third block columns of matrix $\mathbf{N}$ belong to the null-space of $\nabla\boldsymbol{\phi}$, that is,

$$\mathbf{N}^T(\nabla\boldsymbol{\phi})^T = \left\{ \begin{array}{c} \mathbf{0} \\ \boldsymbol{x}_2 - \boldsymbol{x}_1 \\ \mathbf{0} \end{array} \right\},$$

which allows us to solve the constrained system of equations $\hat{\boldsymbol{g}} = \mathbf{0}$ as the following unconstrained system which contains a reduced set of variables:

$$\tilde{\boldsymbol{g}} := \mathbf{N}^T \hat{\boldsymbol{g}} = \mathbf{0}.$$

The second block of equations in $\mathbf{N}^T \hat{\boldsymbol{g}}$, conjugate to $\delta\lambda$, corresponds to solving the equation $(\boldsymbol{x}_2 - \boldsymbol{x}_1)^T(\boldsymbol{g}_3^e + \boldsymbol{g}_3^v) = 0$, which imposes equilibrium of forces along the direction $\boldsymbol{x}_1 - \boldsymbol{x}_2$. Other applications of the null-space method to solve constrained systems of equations in the context of contact and multibody dynamics can be found in [38, 39].

The Jacobian of the reduced residual $\tilde{\boldsymbol{g}}$ is then equal to:

$$\tilde{\mathbf{K}} = \mathbf{N}^T \hat{\mathbf{K}} \mathbf{N} + \mathbf{K}_N, \tag{2.11}$$

where $\mathbf{K}_N$ stems from the linearisation of matrix $\mathbf{N}$ and is equal to:

$$\mathbf{K}_N = \begin{bmatrix} \mathbf{0} & -\hat{\boldsymbol{g}}_3 & \mathbf{0} \\ -\hat{\boldsymbol{g}}_3^T & 0 & \hat{\boldsymbol{g}}_3^T \\ \mathbf{0} & \hat{\boldsymbol{g}}_3 & \mathbf{0} \end{bmatrix}.$$

We note that we could alternatively define a constraint function solely dependent on $\boldsymbol{x}_1$, $\boldsymbol{x}_2$ and $\boldsymbol{x}_3$ such as,

$$\hat{\boldsymbol{\phi}} := \left(\mathbf{I} - \frac{(\boldsymbol{x}_3 - \boldsymbol{x}_1) \otimes (\boldsymbol{x}_2 - \boldsymbol{x}_1)}{\|\boldsymbol{x}_3 - \boldsymbol{x}_1\| \, \|\boldsymbol{x}_2 - \boldsymbol{x}_1\|} \right) (\boldsymbol{x}_3 - \boldsymbol{x}_1),$$

and construct an alternative matrix $\hat{\mathbf{N}}$ such that $\hat{\mathbf{N}}^T (\nabla \hat{\boldsymbol{\phi}})^T = \mathbf{0}$. In this manner, we would eliminate the equation conjugate to $\delta\lambda$ and avoid using an additional variable λ. We have instead kept this variable and used the reduction of the two bar system described above to ease the expression of $\mathbf{N}$ and better deduce from λ the elastic and viscous parts of the displacements. Furthermore, since the variable λ is internal to each viscoelastic element, it can be statically condensed, as it will be described next.

2.1.4 Static condensation of variable λ

We aim to further reduce the total number of dof of the elements by condensing the internal variable λ. By using the following notation:

$$\tilde{\boldsymbol{g}} = \begin{Bmatrix} \tilde{\boldsymbol{g}}_1 \\ \tilde{g}_\lambda \\ \tilde{\boldsymbol{g}}_2 \end{Bmatrix}$$

$$\tilde{\mathbf{K}} = \begin{bmatrix} \tilde{\mathbf{K}}_{11} & \tilde{\mathbf{K}}_{1\lambda} & \tilde{\mathbf{K}}_{12} \\ \tilde{\mathbf{K}}_{\lambda 1} & \tilde{K}_{\lambda\lambda} & \tilde{\mathbf{K}}_{\lambda 2} \\ \tilde{\mathbf{K}}_{21} & \tilde{\mathbf{K}}_{2\lambda} & \tilde{\mathbf{K}}_{22} \end{bmatrix},$$

the static condensation may be achieved by eliminating from the second block of rows of equation

$$\tilde{\mathbf{K}} D \left\{ \begin{array}{c} \boldsymbol{x}_1 \\ \lambda \\ \boldsymbol{x}_2 \end{array} \right\} = -\tilde{\boldsymbol{g}}, \tag{2.12}$$

the variable $D\lambda$ as follows:

$$D\lambda = \tilde{K}_{\lambda\lambda}^{-1} \left(-\tilde{g}_\lambda - \tilde{\mathbf{K}}_{\lambda 1} D\boldsymbol{x}_1 - \tilde{\mathbf{K}}_{\lambda 2} D\boldsymbol{x}_2 \right). \tag{2.13}$$

Replacing this expression back into (2.12) yields the following reduced system of equations:

$$\mathbf{K}\ D \left\{ \begin{array}{c} \boldsymbol{x}_1 \\ \boldsymbol{x}_2 \end{array} \right\} = -\boldsymbol{g},$$

where the vector $\boldsymbol{g}$ and Jacobian $\mathbf{K}$ are given by:

$$\boldsymbol{g} = \left\{ \begin{array}{c} \tilde{\boldsymbol{g}}_1 - \tilde{K}_{\lambda\lambda}^{-1} \tilde{\mathbf{K}}_{1\lambda} \tilde{g}_\lambda \\ \tilde{\boldsymbol{g}}_2 - \tilde{K}_{\lambda\lambda}^{-1} \tilde{\mathbf{K}}_{2\lambda} \tilde{g}_\lambda \end{array} \right\} \tag{2.14}$$

$$\mathbf{K} = \left[\begin{array}{cc} \tilde{\mathbf{K}}_{11} - \tilde{K}_{\lambda\lambda}^{-1} \tilde{\mathbf{K}}_{1\lambda} \tilde{\mathbf{K}}_{\lambda 1} & \tilde{\mathbf{K}}_{12} - \tilde{K}_{\lambda\lambda}^{-1} \tilde{\mathbf{K}}_{1\lambda} \tilde{\mathbf{K}}_{\lambda 2} \\ \tilde{\mathbf{K}}_{21} - \tilde{K}_{\lambda\lambda}^{-1} \tilde{\mathbf{K}}_{2\lambda} \tilde{\mathbf{K}}_{\lambda 1} & \tilde{\mathbf{K}}_{22} - \tilde{K}_{\lambda\lambda}^{-1} \tilde{\mathbf{K}}_{2\lambda} \tilde{\mathbf{K}}_{\lambda 2} \end{array} \right]. \tag{2.15}$$

Note that from equation (2.13) we can update λ from the iterative values $D\boldsymbol{x}_1$ and $D\boldsymbol{x}_2$ as $\lambda^{k+1} = \lambda^k + D\lambda$.

The residual vector $\boldsymbol{g}$ corresponds to the nodal forces of a two noded bar element that has been constructed by algebraically manipulating its initially uncoupled elastic and viscous rheological laws. The general form of the latter will be now particularised to common linear laws and to other more sophisticated cases.

2.1.5 Application to linear and non-linear constitutive laws

Elastic element with linear law

The total elastic energy of a bar of total initial length L is determined in this case by the following quadratic potential energy,

$$V = \frac{L}{2} k (\varepsilon^e)^2, \tag{2.16}$$

with ε^e the elastic strain defined in equation (2.5). We note that since $L = \|\boldsymbol{X}_1 - \boldsymbol{X}_2\| \neq L^e = \|\boldsymbol{X}_1 - \boldsymbol{X}_3\|$, the elastic strain ε^e differs from the total strain, and also from the standard strain of the reduced element between node $\boldsymbol{x}_1$ and $\boldsymbol{x}_3$, which is given by $\varepsilon^* = (l^e - L^e)/L^e$. However, the relation between the latter and ε^e may be deduced as

$$\varepsilon^e = \frac{l_{n+1}^e - L^e}{L} = \lambda_0 \frac{l_{n+1}^e - L^e}{L^e} = \lambda_0 \varepsilon^*,$$

where λ_0 is the value of parameter λ at the initial time t_0. The value of λ_0 does not affect the resulting elastic and viscous strains and stresses, as we have numerically verified. In our numerical tests we will use $\lambda_0 = 0.5$. For clarity, in the remaining expressions, we will remove the subscript $n+1$.

The elastic stress is given by $\sigma^e = \partial V/\partial \varepsilon^e = k\varepsilon^e$, while the elastic contribution to the bar residual, computed as $\boldsymbol{g}^e = \nabla_x V$, is explicitly given by,

$$\boldsymbol{g}^e = k\varepsilon^e \boldsymbol{e}_{13} = \left\{ \begin{array}{c} \boldsymbol{g}_1^e \\ \boldsymbol{g}_3^e \end{array} \right\}, \tag{2.17}$$

where we have defined the vector $\boldsymbol{e}_{ij}$ as

$$\boldsymbol{e}_{ij} = \frac{1}{\|\boldsymbol{x}_i - \boldsymbol{x}_j\|} \left\{ \begin{array}{c} \boldsymbol{x}_i - \boldsymbol{x}_j \\ \boldsymbol{x}_j - \boldsymbol{x}_i \end{array} \right\}.$$

We emphasise that the relation between σ and ε^e is linear, but that the resulting residuals are non-linear due to the relation between l^e and $\boldsymbol{x}_1, \boldsymbol{x}_3$. After the assembling process, the resulting set of equations will be solved with a full Newton-Raphson procedure. This requires the computation of the Jacobain matrix, which is given by,

$$\mathbf{K}^e = k\frac{L^e}{Ll^e}\boldsymbol{e}_{13} \otimes \boldsymbol{e}_{13} + k\frac{\varepsilon^e}{l^e} \left[\begin{array}{cc} \mathbf{I} & -\mathbf{I} \\ -\mathbf{I} & \mathbf{I} \end{array} \right] = \left[\begin{array}{cc} \mathbf{K}_{11}^e & \mathbf{K}_{13}^e \\ \mathbf{K}_{31}^e & \mathbf{K}_{33}^e \end{array} \right].$$

Elastic element with exponential law

Experiments on soft tissues have shown that the stiffness follows a exponential law with respect to the strains [22]. In order to account for the phenomenology of this biological scenario we adopt an elastic potential of the type:

$$V = \frac{Lk_0}{2\alpha}\left(1 - e^{-\alpha(\varepsilon^e)^2}\right). \tag{2.18}$$

with $\alpha > 0$ parameter depending on the material properties. By using this function, the total stored elastic energy remains bounded, and after a given maximum absolute value of the strain, the total elastic energy remains practically unchanged. The corresponding elastic stress is in this case given by,

$$\sigma_{el} = \frac{\partial V}{\partial \varepsilon^e} = k_0 \varepsilon^e e^{-\alpha(\varepsilon^e)^2}. \tag{2.19}$$

It is worth highlighting that stress law in equation (2.19) can also be interpreted in terms of a linear elastic material with a non-linear *effective stiffness* $k = k_0 e^{-\alpha\varepsilon^2}$ and stress-strain constitutive law $\sigma^e = k\varepsilon^e$. We note that the reversible softening that such a potential induces is also in agreement with experimental measurements of actin networks [40]. We do not attempt to physically explain at the nano-scale the source of this softening, but we do aim to test rheological laws that can reproduce at the micro-scale such behaviour.

When comparing the quadratic and exponential elastic potentials in (2.16) and (2.24), it can be deduced that while in the former case the stored elastic

energy is unbounded, in the latter case function V is limited. Figure 2.2a shows the two kind of functions V, and in the exponential case, for two values of α, which shows that the larger is α, the lower is the maximum stored elastic energy. Figure 2.2b shows the corresponding stresses derived from the potential functions. As it can be observed, the limitation on the maximum value of V also implies that the elastic stress does not monotonically increase, but is eventually reduced as ε^e increases.

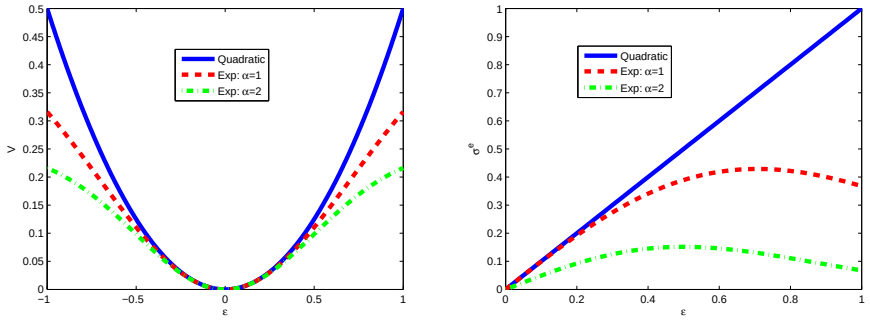

(a) (b)

Figure 2.2: (a) Elastic potential V: quadratic function and exponential function with $\alpha = 1, 2$. (b) Corresponding stresses σ^e.

It is also worth pointing out that for a system of E bars, each one with elastic energy $V^j, j = 1, \ldots, E$, the minimisation of the elastic equilibrium, which is equivalent to the minimisation of the total elastic energy $\sum_j V^j$, is also equivalent to the maximisation of the sum of the total effective stiffness k_{TOT} measured as

$$k_{TOT} = \sum_{j=1}^{E} L^j k^j = \sum_{j=1}^{E} L^j k_0 e^{-\alpha(\varepsilon_j^e)^2}, \tag{2.20}$$

where ε_j^e is the elastic strain and initial stiffness of bar j. This fact can be verified by noting that $2\alpha\nabla_x V = -\nabla_x k_{TOT}$.

The contribution to the residual and the stiffness matrix of an elastic bar with nodal ends in $\boldsymbol{x}_1$ and $\boldsymbol{x}_3$ is therefore,

$$\boldsymbol{g}^e = k_0 \varepsilon^e e^{-\alpha(\varepsilon^e)^2} \boldsymbol{e}_{13},$$
$$\mathbf{K}^e = \frac{k_0}{l^e} e^{-\alpha(\varepsilon^e)^2} \varepsilon^e \begin{bmatrix} \mathbf{I} & -\mathbf{I} \\ -\mathbf{I} & \mathbf{I} \end{bmatrix} + \frac{k_0}{L} e^{-\alpha(\varepsilon^e)^2} \left(\frac{L^e}{l^e} - 2\alpha(\varepsilon^e)^2 \right) \boldsymbol{e}_{13} \otimes \boldsymbol{e}_{13}.$$

Viscous element with linear law

The residual stress of the viscous element with viscosity η is equal to $\sigma^v = \eta \dot{\varepsilon}^v$, which acts along the direction $\boldsymbol{x}_2 - \boldsymbol{x}_3$, and with $\varepsilon_{n+1}^v = \frac{l_{n+1}^v - L^v}{L}$ the viscous

strain. The viscous contribution to the total residual is then given by,

$$\boldsymbol{g}^v = \eta \dot{\varepsilon}^v \boldsymbol{e}_{32}. \tag{2.21}$$

This contribution will be discretised in time by employing the time-step size $\Delta t = t_{n+1} - t_n$ and the following time-stepping,

$$\boldsymbol{g}^v_{n+\theta} = \eta \frac{l^v_{n+1} - l^v_n}{L\Delta t} \boldsymbol{e}_{32,n+\theta} = \lambda_0 \eta \frac{l^v_{n+1} - l^v_n}{L^v \Delta t} \boldsymbol{e}_{32,n+\theta}, \tag{2.22}$$

where

$$\begin{aligned} l^v_{n+\theta} &= \|\boldsymbol{x}_{2,n+\theta} - \boldsymbol{x}_{3,n+\theta}\|, \\ l^v_n &= \|\boldsymbol{x}_{2,n} - \boldsymbol{x}_{3,n}\|, \\ \boldsymbol{g}^v_{n+\theta} &= (1-\theta)\boldsymbol{g}^v_n + \theta \boldsymbol{g}^v_{n+1}, \\ \boldsymbol{e}_{i,n+\theta} &= (1-\theta)\boldsymbol{e}_{i,n} + \theta \boldsymbol{e}_{i,n+1}, \end{aligned}$$

with $\theta \in [0,1]$ an algorithmic parameter. For $\theta = 0$ and $\theta = 1$ we recover the backward and forward Euler time-stepping algorithms. From equation (2.22), it follows that the load contribution at time t_{n+1}, to be assembled together with the elastic part deduced in Sections 2.1.5 or 2.1.5, reads

$$\boldsymbol{g}^v_{n+1} = \frac{\theta - 1}{\theta} \boldsymbol{g}^v_n + \frac{\eta}{\theta L} \frac{l^v_{n+1} - l^v_n}{\Delta t} \boldsymbol{e}_{32,n+\theta} = \left\{ \begin{array}{c} \boldsymbol{g}^v_3 \\ \boldsymbol{g}^v_2 \end{array} \right\}. \tag{2.23}$$

For the particular case when $\theta = 0$, the current viscous length l^v_{n+1} may be derived from the previous residual contribution $\boldsymbol{g}^v_n$ and equation (2.22). In all other cases, the solution of a non-linear system of equations is required, which may be solved by using the following corresponding Jacobian:

$$\begin{aligned} \mathbf{K}^v =& \frac{\eta}{\theta L \Delta t} \boldsymbol{e}_{32,n+\theta} \otimes \boldsymbol{e}_{32,n+1} - \frac{\eta}{L\Delta t} \frac{l^v_{n+1} - l^v_n}{l^v_{n+\theta}} \boldsymbol{e}_{32,n+\theta} \otimes \boldsymbol{e}_{32,n+\theta} \\ &+ \frac{\eta}{L\Delta t} \frac{l^v_{n+1} - l^v_n}{l^v_{n+\theta}} \left[\begin{array}{cc} \mathbf{I} & -\mathbf{I} \\ -\mathbf{I} & \mathbf{I} \end{array} \right] = \left[\begin{array}{cc} \mathbf{K}^v_{33} & \mathbf{K}^v_{32} \\ \mathbf{K}^v_{23} & \mathbf{K}^v_{22} \end{array} \right]. \end{aligned}$$

Viscous element with exponential law

Similarly to the elastic case, it has been experimentally observed that the material viscosity may decresase after an imposed stretching process [22]. In order to mimic such a behaviour at the micro-scale level, we suggest the following non-linear viscous law:

$$\boldsymbol{g}^v = \eta_0 e^{-\beta(\varepsilon^v)^2} \dot{\varepsilon}^v \boldsymbol{e}_{32} \tag{2.24}$$

In this case, the factor $\eta = \eta_0 \exp^{-\beta(\varepsilon^v)^2}$ has the role of strain-dependent effective viscosity that decreases as the viscous strain increases. The time integration of the previous equation is resolved resorting again to a $\theta-$averaged time-stepping,

$$\boldsymbol{g}^v_{n+\theta} = \eta_0 e^{-\beta(\varepsilon^v_{n+\theta})^2} \frac{\Delta \varepsilon^v}{\Delta t} \boldsymbol{e}_{32,n+\theta}$$

As a result, the internal force vector and the associated Jacobian read,

$$
\begin{aligned}
\boldsymbol{g}^v_{n+1} &= \frac{\theta-1}{\theta}\boldsymbol{g}^v_n + \frac{\eta_0}{\theta L\Delta t} e^{-\beta(\varepsilon^v_{n+\theta})^2}(l^v_{n+1}-l^v_n)\boldsymbol{e}_{32,n+\theta} \\
\mathbf{K}^v =& e^{-\beta(\varepsilon^v_{n+\theta})^2}\frac{\eta_0}{\theta L\Delta t}\boldsymbol{e}_{32,n+\theta}\otimes\boldsymbol{e}_{32,n+1} \\
&- e^{-\beta(\varepsilon^v_{n+\theta})^2}\frac{\eta_0}{L\Delta t}(l^v_{n+1}-l^v_n)\left(\frac{1}{l^v_{n+\theta}}+\frac{2\beta\varepsilon^v_{n+\theta}}{L}\right)\boldsymbol{e}_{32,n+\theta}\otimes\boldsymbol{e}_{32,n+\theta} \\
&+ e^{-\beta(\varepsilon^v_{n+\theta})^2}\frac{\eta_0}{L\Delta t}\frac{l^v_{n+1}-l^v_n}{l^v_{n+\theta}}\begin{bmatrix}\mathbf{I} & -\mathbf{I}\\ -\mathbf{I} & \mathbf{I}\end{bmatrix}
\end{aligned}
$$

2.2 The Kelvin (Voigt) model

The Kelvin model is shown in Fig 2.3a where a spring element(purely elastic) and dashpot element(one purely viscous) are connected in parallel. The spring

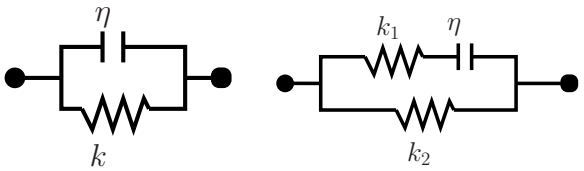

(a) (b)

Figure 2.3: (a)The Kelvin model.(b)The generalised Maxwell model.

and dashpot element have the following strees-strain relations according to 2.1:

$$\sigma^e = E\epsilon \tag{2.25}$$

$$\sigma^v = \eta\dot{\epsilon} \tag{2.26}$$

with k and η the material stiffness and viscosity, respectively. The modelling of Voigt elements does not represent major difficulties, since it corresponds to the superposition of the elastic and viscous stresses(2.27), with $\epsilon^e = \epsilon^v$.

$$\sigma = \sigma^e + \sigma^v \tag{2.27}$$

The same models previously described in section 2.3 may be employed for the Kelvin element, replacing in the linear case, x_3 by x_2, and in the viscous case x_3 by x_1.

2.3 The generalised Maxwell model

The Maxwell and Kelvin models are the simplest, two-element models. More realistic material responses can be modelled using more elements. The generalised Maxwell model is shown in Fig 2.3b, is a three element model that effectively combines the Maxwell Model and a spring in parallel. A viscous material is modeled as a spring and a dashpot in series with each other, both of which are in parallel with a lone spring.
In order to model this system, the following physical relations must be realized:

For parallel components:

$$\sigma_{tot} = \sigma_1 + \sigma_2 \qquad \text{and} \qquad \epsilon_{tot} = \epsilon_1 = \epsilon_2 \tag{2.28}$$

For series components:

$$\sigma_{tot} = \sigma_1 = \sigma_2 \qquad \text{and} \qquad \epsilon_{tot} = \epsilon_1 + \epsilon_2 \tag{2.29}$$

These relationships help relate the various stresses and strains in the overall system and the Maxwell arm:

$$\sigma_{tot} = \sigma^m + \sigma_1^e \tag{2.30}$$

$$\epsilon_{tot} = \epsilon^m = \epsilon_1^e \tag{2.31}$$

$$\sigma^m = \sigma^v = \sigma_2^e \tag{2.32}$$

$$\epsilon^m = \epsilon^v + \epsilon_2^e \tag{2.33}$$

where the subscripts 1 and 2 denote the first and second spring, and the superscripts m, v, e refer to Maxwell, viscous and elastic components respectively.

The corresponding viscous Jacobian matrix K^v, elastic Jacobian matrix K^e, viscous stress vector g^v and elastic stress vector g^e of the generalized Maxwell model can be obtained by superposition of the Maxwell model (section 2.1) and a single spring model (purely elastic), in parallel.

2.4 Stress recovery

The main aim of this section is to get a distribution of the stress field. In order to obtain the stress values, we have two options:

(**i**) Using the nodal displacement u: Having obtained the nodal displacement for each truss element, stress values are to be calculated from the derivatives of the displacement (strains), which in our case would be discontinuous. In this

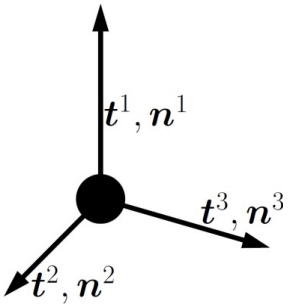

Figure 2.4: The bar elements connected to the node.

case, we would require to compute a continuous strain field $\epsilon(u)$, and retrieve the stress, from an assumed strain-stress relationship for the solid elements. Therefore, due to the non-linearities of the material which is modeled with trusses, it is not easy to deduce a valid strain-stress relationship.

(**ii**) Using the elemental truction $\boldsymbol{t}$: In this work, we assume that the tractions result from a nodal stress, i.e $\boldsymbol{t} = \boldsymbol{\sigma n}$ with $\boldsymbol{n} = \begin{pmatrix} n_x & n_y & n_z \end{pmatrix}$ as the vector director. This relation may not be satisfied for all elements connected to the node. Hence, we will use the following definition of the error between the nodal stress $\hat{\boldsymbol{\sigma}}$ and the all elemental tructions $\boldsymbol{t}^i$ acting on a node:

$$E = \sum_{i=1}^{n} ||\boldsymbol{N}^i \hat{\boldsymbol{\sigma}} - \boldsymbol{t}^i||^2 \tag{2.34}$$

where $\boldsymbol{N}$ contains the components of the normal vector and $\hat{\boldsymbol{\sigma}}$ is nodal stresses which are supposed to be determined, n is the number of bar element connected to the node and $\boldsymbol{t}$ is the known traction for each element. For a 2D bar element, $\boldsymbol{N}$ and $\hat{\boldsymbol{\sigma}}$ can be expressed as

$$\boldsymbol{N} = \begin{pmatrix} n_x & n_y & 0 \\ 0 & n_x & n_y \end{pmatrix} \tag{2.35}$$

$$\hat{\boldsymbol{\sigma}} = \begin{pmatrix} \sigma_{xx} \\ \sigma_{xy} \\ \sigma_{yy} \end{pmatrix} \tag{2.36}$$

We will evaluate $\hat{\boldsymbol{\sigma}}$ by the minimizing this error. The minimization of the equation (2.34) gives,

$$\boldsymbol{A}\hat{\boldsymbol{\sigma}} = \boldsymbol{b} \tag{2.37}$$

where

$$\boldsymbol{A} = \sum_{i=1}^{n} \boldsymbol{N}^{i^T} \boldsymbol{N}^i \tag{2.38}$$

$$\boldsymbol{b} = \sum_{i=1}^{n} \boldsymbol{N}^{i^T} \boldsymbol{t}^i \tag{2.39}$$

The above one can be solved to get unknowns $\hat{\boldsymbol{\sigma}}$ as follows:

$$\hat{\boldsymbol{\sigma}} = \boldsymbol{A}^{-1} \boldsymbol{b} \tag{2.40}$$

Proposition 1: The solution of the above equation is unique, if the vectors director $\boldsymbol{n}^i$ of the elements connected to the node span $\mathbb{R}^d$, with d the space dimensions.

Proof: See appendix A.

Chapter 3

Results

In all the subsequent examples the non-linear equations are solved with $\theta = 0.5$, which has ensured in all cases numerically stable results.
All analyses were conducted using the following software: MATLAB R2011a, Gid.10.1.4d.

3.1 One dimension bar element

3.1.1 Creep of one bar element - Linear elasticity

We first compare the solutions of a generalised Maxwell bar element using a linear viscoelastic rheological law. A unit length bar is stretched by fixing the left end of the bar and applying a triangular load profile at the right end, as shown in Figure 3.1 a. The material properties employed are $k_0 = \eta = 1.0$ and $\Delta t = 0.1$, which was sufficient to achieve convergence in 4 iterations per time increment. The resulting horizontal displacements u at the right node when using the monolithic solution process and the null-space are shown in Figure 3.1b, which exactly coincide. The trend of the displacements history after time $t = 2$ reproduce the common creep process that takes place for a fixed applied stress. In our case the strain approaches asymptomatically the zero value.

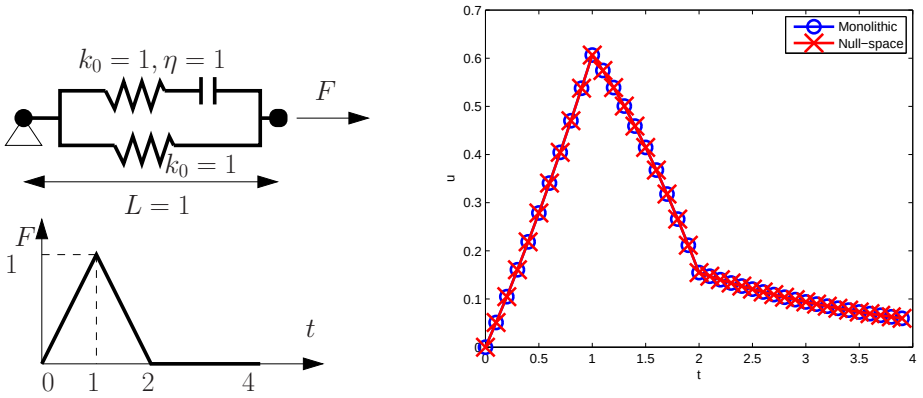

(a) (b)

Figure 3.1: 1 bar element with an applied load. (a) Geometry, material properties and boundary conditions. (b) Displacement of the right node.

3.1.2 Stress relaxation of one bar element - Exponential elasticity

It has been experimentally tested that the network of actin filaments softens after a pre-stretch is applied, while the viscosity decreases, but to a lesser extent [22]. Furthermore, after a given period of time (independent of the amount of pre-stretch), the material recovers the initial elastic and viscous properties.

We have reproduced this behaviour by using the exponential law presented in Subsection 3.3.5. A single bar element with Maxwell rheological behaviour undergoes a prescribed strain imposed by the displacement history shown in Figure 3.2a. As indicated by the resulting stiffness in equation (2.19), the effective stiffness decreases as ε^e increases, and this reduction is more pronounced as the material parameter α increases.

As it can be observed in Figure 3.2b, the effective stiffness $k = k_0 e^{-\alpha(\varepsilon^e)^2}$ decreases when α increases from 1 to 100 during the times that the elastic strain is larger. For $t > 2$ the global bar remains undeformed while stresses asymptotically recover their original value in a time interval of the order of the unity. It is worth observing that a behaviour of this sort can be experimentally observed when performing stretch cycles on *in vitro* epithelial-cell layers [22], although with a recovery time considerably longer than those here achievable *in silico* when adopting the non-linear Maxwell element shown in Figure 3.2.

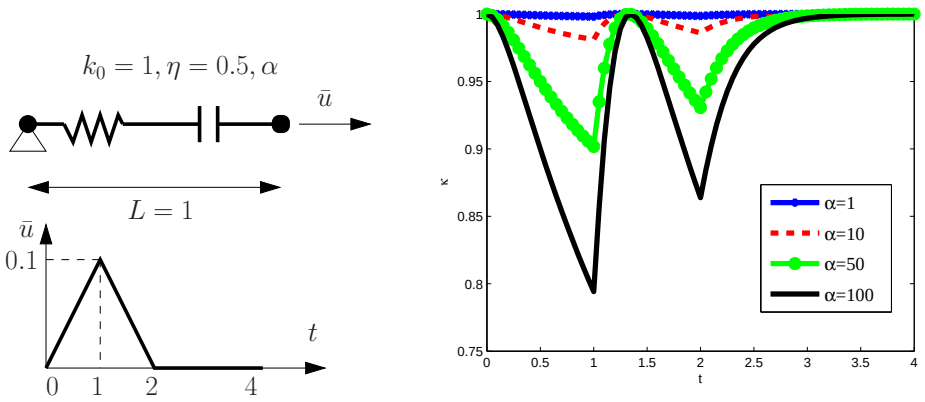

(a) (b)

Figure 3.2: 1 bar element with constrained displacements. (a) Geometry, material properties and boundary conditions. (b) Value of the effective stiffness $k = k_0 e^{-\alpha(\varepsilon^e)^2}$.

3.1.3 Bar element with non-linear viscosity

In order to model the drop in viscosity observed and quantified in [22] when an epithelial-cell layer is subject to a stretching cycle, we will apply the non-linear viscous law given in equation (2.24), and test the effects that the value of the material parameter β has on the evolution of the effective viscosity η. We have used one single bar element subjected to the same boundary conditions applied in the previous example, with $k_0 = 1$, $\eta_0 = 1$ and $\alpha = 100$ (see Figure 3.3).

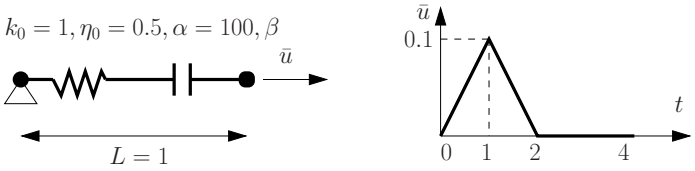

Figure 3.3: 1 bar element with constrained displacements. Geometry, material properties and boundary conditions.

Figure 3.4 shows the evolution of the effective stiffness and viscosity when $\beta = 0$ (linear viscosity) and $\beta = 100$. While in the former case the values are exactly to those tested in the previous example with $\alpha = 100$ (constant viscosity), in the latter case the viscosity is reduced by 40%. More importantly, the variation of α has minimal effects on the evolution of the effective stiffness, which allows to fit the parameters α and β independently.

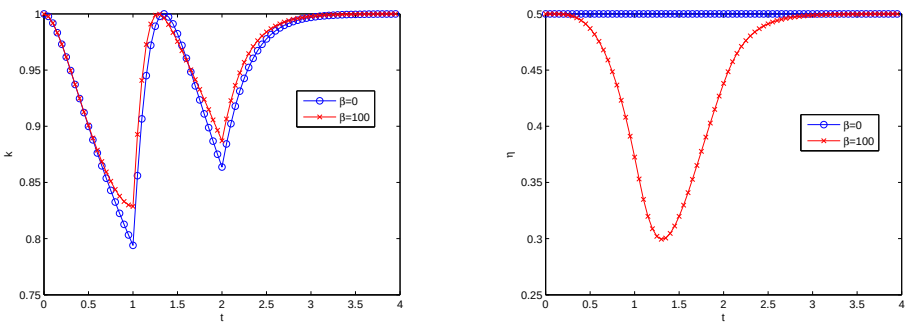

(a) (b)

Figure 3.4: 1 bar element with non-linear viscosity. Evolution of (a) the effective viscosity $\eta = \eta_0 e^{-\beta(\varepsilon^v)^2}$ and (b) the effective stiffness $k = k_0 e^{-\alpha(\varepsilon^e)^2}$, for different values β.

3.2 Two dimensional elastic square

In this section, two dimensional test cases are presented in order to check the convergence of the method using different meshes. Since the continua and truss system are different problems, the convergence should not be expected but we can measure the degree of discrepancy. By neglecting the deformation and stress respect to viscous part, the elastic behavior of the tissues are only considered in this example based on the Kelvin model. The linear constitutive law as the example of section 3.1.1 is implemented here for the bar elements.

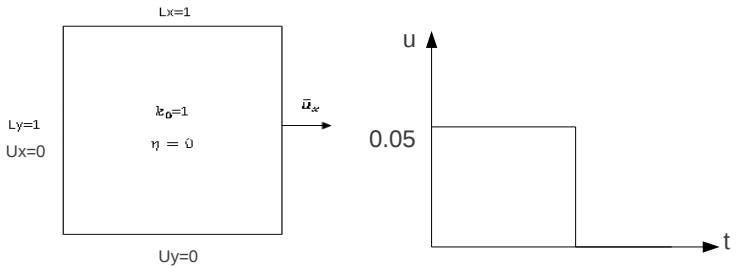

(a) (b)

Figure 3.5: Dirichlet boundary conditions.

The material properties employed are $k_0 = 1$, $\eta = 0$ and $\Delta t = 0.025$ which was sufficient to achieve convergence in 3 iterations per time increment. As

shown in Figure 3.5a, a unique square domain is assumed for this test with a defined displacement $\bar{u}$= 0.05 and applying a step loading (Figure 3.5 b) along the x direction. The domain has been constructed by meshing with triangle and converting the edges of the triangle into bar elements. Two different meshes types M_1 and M_2 are created while for each one four mesh sizes $h = 0.5$, 0.25, 0.1 and 0.05 are assumed (Figure 3.6).

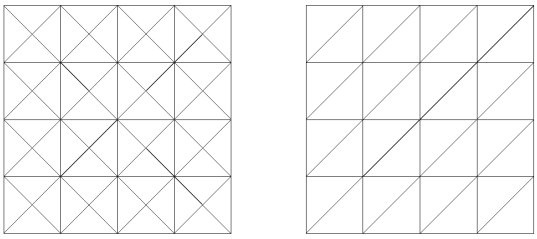

(a) Mesh M_1 (b) Mesh M_2

Figure 3.6: Implemented meshes with $h = 0.25$

The obtained nodal stress values (see section 2.6 for the details) of the first increment corresponding to different meshes are shown in Figure 3.8. It can be observed that despite the fact that the computed stresses has the same trend as the analytical solution, some discrepancy exist.

In order to recover this discrepancy, we will use E^i as the nodal error at node i (the difference between the recovered and the analytical stress) obtained from equation (2.34). The corresponding nodal values are printed in Figure 3.9, showing that a suitable level of error is resulted inside the domain for both mesh types M_1 and M_2 and also the error appears to depend on the truss topology. Indeed, the error over the domain E_Ω can be expressed as:

$$E_\Omega = \int_\Omega E(x) d\Omega \tag{3.1}$$

where we use a finite element interpolation to get an error field $E(x)$ from the nodal errors E^i as,

$$E(x) = \sum_i E^i N^i(x) \tag{3.2}$$

with N^i the shape function of node i, and Ω the domain area.

The convergence plot of mentioned error corresponding to the mesh types M_1 and M_2 are presented in Figure 3.7. The truss system and the continuous model are substantially different; therefore, a reduction of the error can not be expected. Nevertheless, the convergence plot shows that the error does not increase as h diminishes for meshes M_1 and M_2.

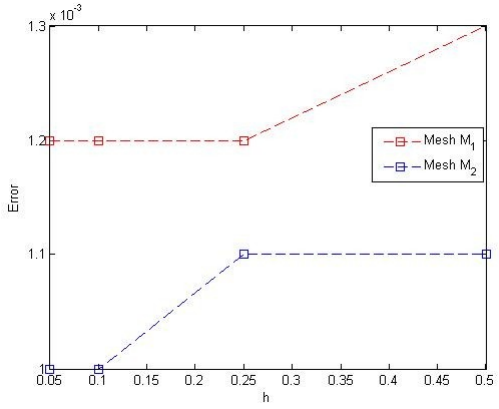

Figure 3.7: Convergence graph

The analysis of the current method for different poisson ratios corresponding to different mesh topologies is out of the scope of this thesis but can be found in [41].

3.3 Three dimension non-linear tissue

The same exponential law used in the example of Section 3.1.2 is now applied to a three-dimensional network of bars that may be reasonably assumed to represent the global actin network crossing through cells in an epithelial tissue. A generic specimen with dimensions $1.0 \times 1.0 \times 0.0625$ and with a prescribed displacement $\bar{u}$ along the x direction has been tested (see Figure 3.10a). The tissue has material properties $k_0 = 1$, $\eta = 0.5$ and $\alpha = 100$, and has been constructed by meshing with tetrahedra the external parallelepiped, and converting the edges of the tetrahedra into bar elements. As a result, we have obtained in total $E = 2473$ bar elements.

Due to the stretching, the material undergoes a softening effect in the x direction. Figure 3.10b shows the deformed configuration with $\bar{u} = 0.1$ at the time if highest strain, together with the contour plot of the values of the effective stiffness $k = k_0 e^{-\alpha(\varepsilon^e)^2}$. As expected, those bars aligned to the x direction have their effective stiffness further reduced than those aligned to the y or z direction.

Figure 3.11a shows for two values of maximum stretch, the evolution of the averaged total effective stiffness k_{TOT}, computed as

$$\bar{k}_{TOT} = \frac{1}{N_b} \sum_{i=1}^{E} k^i.$$

Although the boundary conditions are similar to those in the 1 bar element

of Section 3.1.2, the reduction in $\bar{k}_{TOT}$ is far smaller in the present case. This is due to the fact that the effective stiffness is averaged among all bars, regardless of their orientation, while the applied strain is highly anisotropic. In fact, during the stretching process, some bars have their effective stiffness reduced 49%, while the stiffness of other bars, mostly perpendicular to the stretch, remains nearly unaffected.

Figure 3.11b shows the evolution of the sum of the reactions in the x direction on the moving boundary, denoted by R_x. Due to the softening of the material, the rate R_x decreases when the elastic strain increases. After time $t = 1$, the rate of R_x is in fact recovered, but with opposite sign. When the applied displacement equals zero, the elastic strain progressively reduces to zero, and consequently also does the total reaction, mimicking the stress relaxation process. The overall behaviour is similar to a single viscoelastic Maxwell bar element, but now obtained from a 3D network.

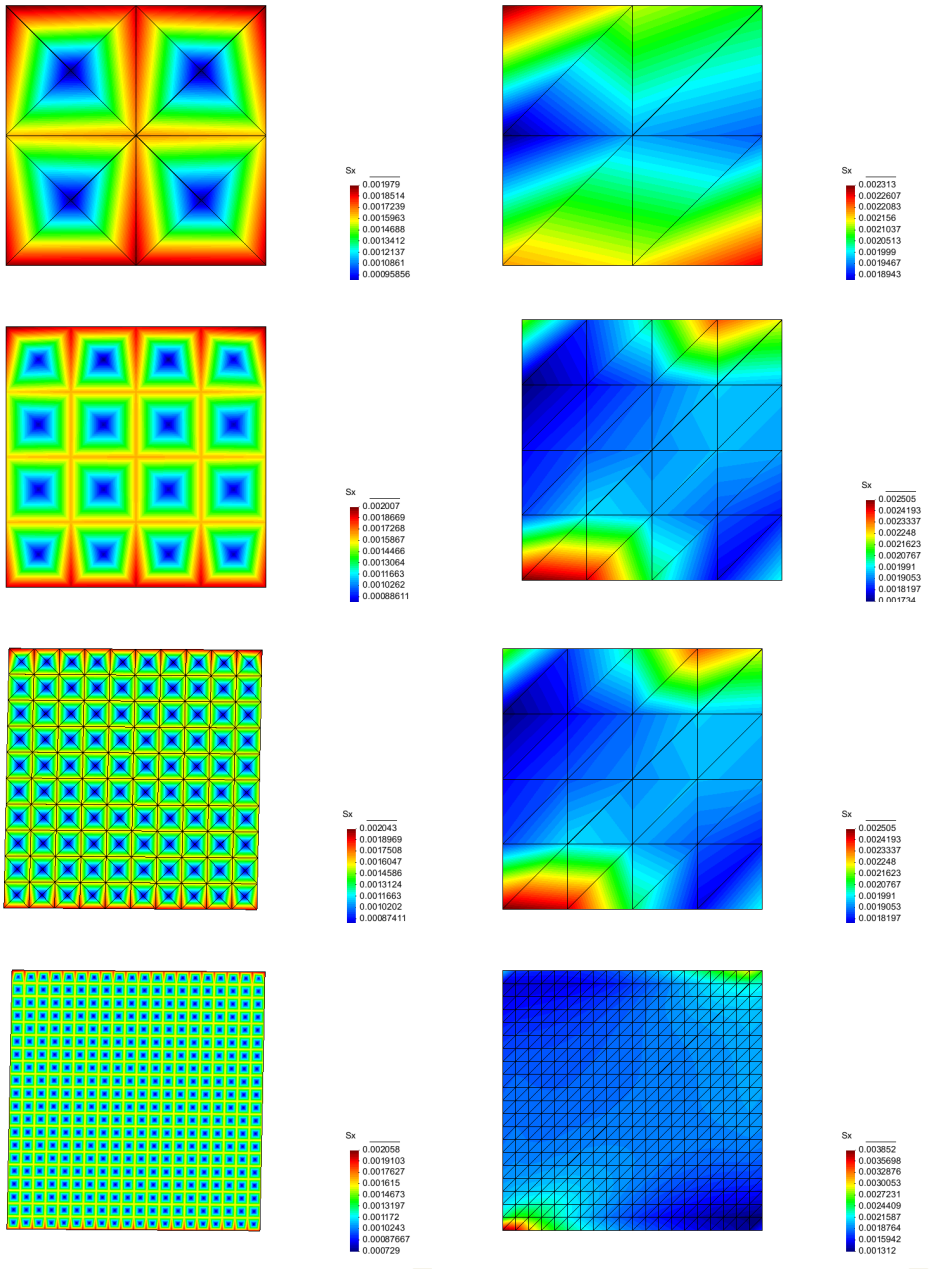

(g) Mesh M_1 with h=0.05

(h) Mesh M_2 with h=0.05

Figure 3.8: contour plots of the computed nodal stress

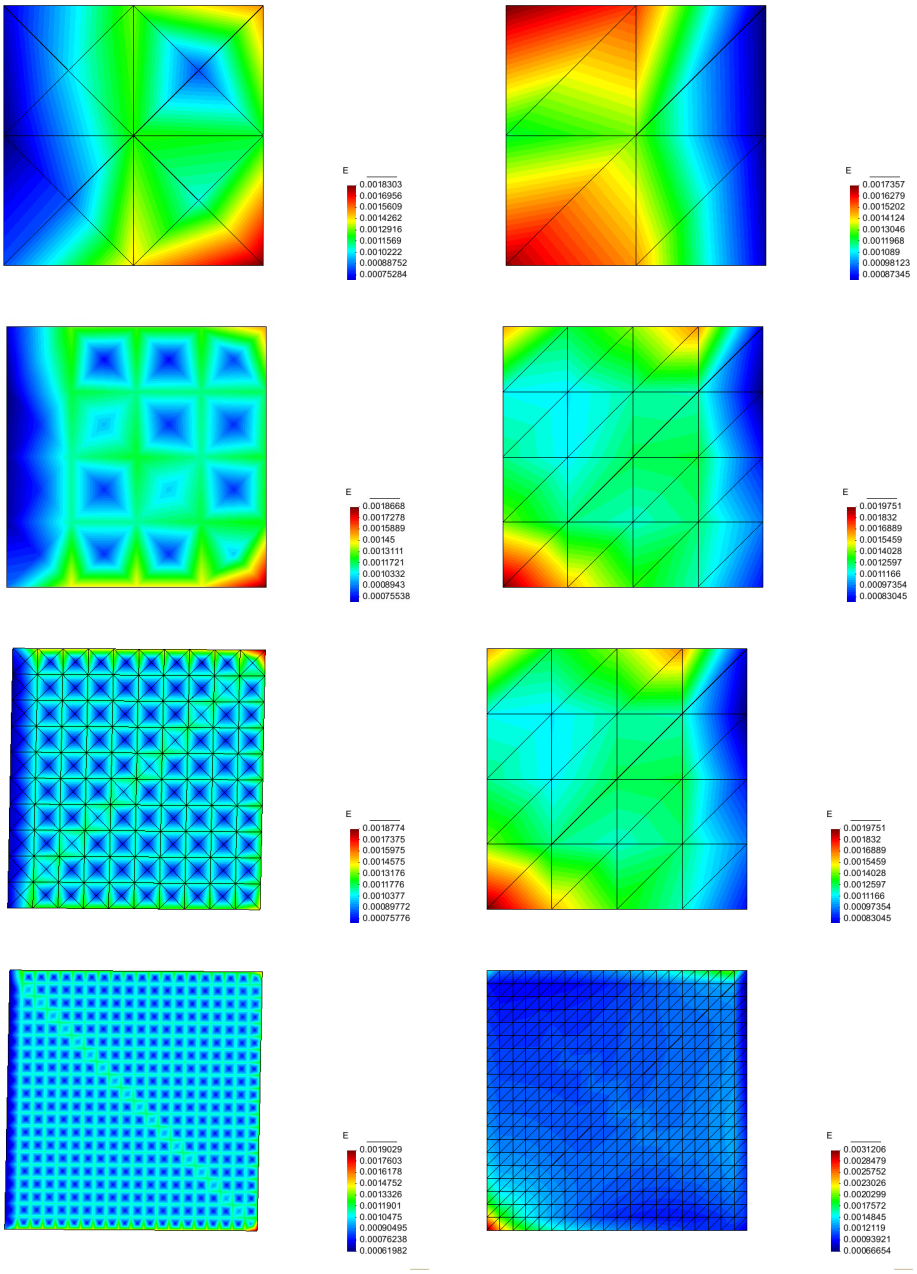

(g) Mesh M_1 with h=0.05

(h) Mesh M_2 with h=0.05

Figure 3.9: contour plots of the computed nodal error

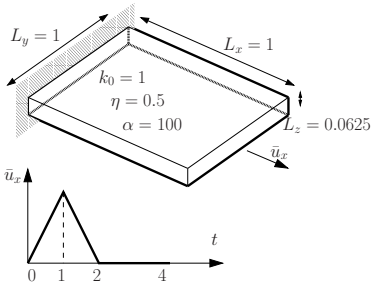

(a)

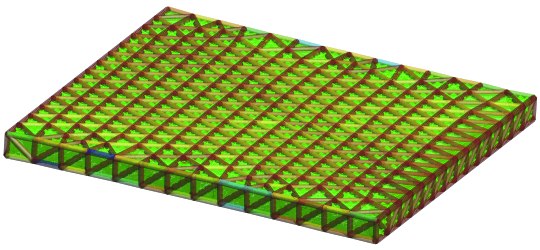

(b)

Figure 3.10: (a) Geometry and boundary conditions of the 3D tissue example. (b) Deformed configuration at $t = 1$, with values of $k = k_0 e^{-\alpha(\varepsilon^e)^2}$ (b), where dark red indicates $k = 1$ and dark blue indicates $k \approx 0.5$.

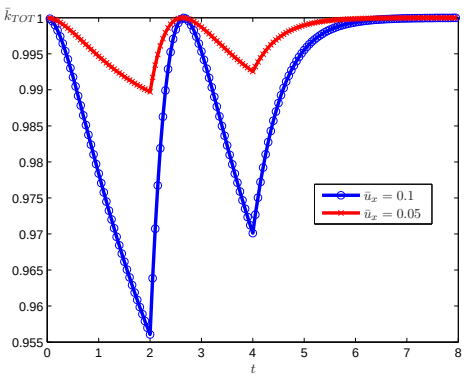

(a)

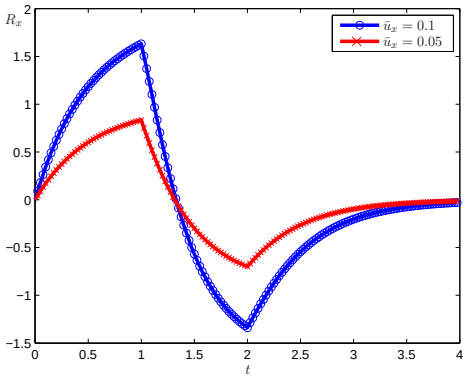

(b)

Figure 3.11: (a) Evolution of total effective stiffness k_{TOT}. (b) Sum of the x component of the reactions on the nodes with prescribed displacement $\bar{u}$.

Chapter 4

Conclusions and further work

We have applied the methodology to model reversible stiffness softening - a non-linear elastic and viscous behaviour that has been experimentally observed in biomechanical tests performed on epithelial lung cell monolayers [22]. We have developed a general framework for the modelling of a viscoelastic material using a system of bars, which can easily handle non-linear constitutive laws. The model was developed to simulate global actin-network dynamics in soft tissues but can be equally applied to other engineering problems, and may be easily extended to include other non-linear effects such as incompressibility constraints or growth. The key ingredient of the formulation is the splitting of the elastic and viscous parts into two parts, which are joined together in a single element by using null-space projection of the constraints and static condensation. Application of the method to both 2D and 3D cases showed this simple model is able to capture the salient properties observed there *in vivo*, that is the reversible softening of the tissue during the stretching process, and the eventual recovery of the initial stiffness.

No topology changes of the network are included in the model. This feature is in fact relevant for the modelling of some morphogenetic movements where some invasive cells replace other regions of the tissue that are absorbed. Some examples are germband extension in Drosophila Melanogaster or epiboly in Zebrafish embryos, or the alignment of fibroblast during the segmentation of Drosophila. In such cases, the other relevant features that have not been included so far are the effect of morphogen concentration onto the cell activity. It has been known that gens are expressed according to the concentration of some proteins (mor-

phogens). This gens are in turn responsible of the cell active deformations, and therefore are part of a mechano-diffusion system. Some recent attempts exist in the literature, where the mechanical model is coupled with diffusion-reaction equations, but not in the context of embryo development. Such possibility may be easily included in the proposed thesis in order to study the still unexplored biomechanical repercussions of such additional concentration field. Indeed, the present model is not sufficient to simulate the change of the scale, Hence, it can be extended to consider the changes in rest length (remodelling) to match recovery time.

Appendix A

Uniqueness Proof

In Section 2.4, it is shown that the unknown stress $\hat{\boldsymbol{\sigma}}$ are defined by minimization of the stress error E, which gives

$$\boldsymbol{A}\hat{\boldsymbol{\sigma}} = \boldsymbol{b}$$

with

$$\boldsymbol{A} = \sum_j \boldsymbol{N}_j^T \boldsymbol{N}_j$$

$$\boldsymbol{b} = \sum_{i=1}^{n} \boldsymbol{N}^{i^T} \boldsymbol{t}^i$$

By definition, matrix A is semi positive definite. Therefore, the uniqness of the solution is equivalent to the following condition:

$$\boldsymbol{\sigma}^T \boldsymbol{A} \boldsymbol{\sigma} = \sum_j \boldsymbol{\sigma} \boldsymbol{n}_j . \boldsymbol{\sigma} \boldsymbol{n}_j = 0 \Rightarrow \boldsymbol{\sigma} = 0 \tag{A.1}$$

But,

$$\sum_j \boldsymbol{\sigma} \boldsymbol{n}_j . \boldsymbol{\sigma} \boldsymbol{n}_j = \sum_j ||\boldsymbol{t}_j||^2 \tag{A.2}$$

So

$$\boldsymbol{\sigma}^T \boldsymbol{A} \boldsymbol{\sigma} = 0 \Rightarrow \boldsymbol{t}_j = 0, \forall j \tag{A.3}$$

i.e., condition A.1 implies that,

$$\boldsymbol{t}_j \cdot \boldsymbol{e}_i = 0, \forall i, j \tag{A.4}$$

Setting $\boldsymbol{n}_j = \alpha_j^k \boldsymbol{e}_k$ we have that,

$$\boldsymbol{t}_j \cdot \boldsymbol{e}_i = \alpha_j^k \boldsymbol{\sigma} \boldsymbol{e}_k \cdot \boldsymbol{e}_i = \sum_k \alpha_j^k \sigma_{ik} \tag{A.5}$$

Therefore, equation (A.3) is equivalent to,

$$\sum_k \alpha_j^k \sigma_{ik} = 0, \forall i, j \tag{A.6}$$

By denoting by $\boldsymbol{\sigma}_i$ the i-th row of the tensor $\boldsymbol{\sigma}$, this condition may be also expressed as,

$$\boldsymbol{n}_j \cdot \boldsymbol{\sigma}_i = 0, \forall i, j \tag{A.7}$$

that is, the vectors $\boldsymbol{n}_j$ are orthogonal to each one of the rows of $\boldsymbol{\sigma}$. If the vectors $\boldsymbol{n}_j$ span the whole space $\mathbb{R}^d$, this is only possible when $\boldsymbol{\sigma}_i = 0$, as we wanted to proof.

Bibliography

[1] Schliwa, M., The cytoskeleton. An introductory survey. (Springer-Verlag, New York, 1986).

[2] Andrews, G. F., The living substance as such; and as organism. J Morph 12 (Suppl.), 1-176 (1897).

[3] Mathews, A. P. Whitcher, B. R., The importance of mechanical shock in protoplasmic activity. Am J Physiol 8, 300-306 (1903).

[4] Chambers, R., Microdissection studies II the cell aster a reversible gelation phenomenon. J Exp Zool 23, 483-505 (1917).

[5] Mast, S. O., Structure, movement, locomotion, and stimulation in amoeba. J Morph Physiol 41, 347- 425 (1926).

[6] Butschli, O., Investigation on microscopic foams and on protoplasm. (A. and C. Black, London, 1894).

[7] Freundlich, H. Bircumshaw, L. L., Ueber das thixotrope Verhalten von Aluminiumhydroxydgelen. Kolloid, Z. 40, 19 (1926).

[8] Abramson, H. A., The mechanism of the acute inflammatory process. Alexanders Colloid Chemistry, Theoretical and Applied 2, 701 (1926).

[9] Angerer, C. A., The effects of mechanical agitation on the relative viscosity of amoeba protoplasm. J Cell Comp Physiol 8, 329-345 (1936).

[10] Roger D. Kamm and Mohammad R. K. Mofrad. Introduction, with the biological basis for cell mechanics.

[11] Rosso R., Virga E. G Adhesive borders of lipid membranes Proc.R Soc.Lond A 455 , 4145–4168 (1999).

[12] Sen S, Subramanian S, Discher DE. Indentation and adhesive probing of a cell membrane with AFM: theoretical model and experiments, Biophysical J., 2005. 89(5): 3203-3213.

[13] Sultan, C., Stamenovic, D., Ingber, D.E., A Computational Tensegrity Model Explains Dynamic Rheological Behaviors of Living Cells, Annals of Biomedical Engineering, Vol. 32(4), 520-530, 2004.

[14] Helfrich.W. Elastic properties of lipid bilayers: Theory and possible experiments. Z. Naturforsch. Teil C, 28:693703, 1973.

[15] L.B. Freund and Y. Lin, The role of binder mobility in spontaneous adhesive contact and implications for cell adhesion. J Mech Phys Solids, 52 (2004).

[16] Suvranu De. Farshid Guilak, mohammad mofrad, Computational Modeling in biomechanics.

[17] Vogel, V. Sheetz, M. Local force and geometry sensing regulate cell functions. Nature Rev. Mol. Cell Biol. 7, (2006), 265275.

[18] Ingber, D. E. Tensegrity, I. I. How structural networks influence cellular information processing networks. J. Cell Sci. 116,(2003), 13971408.

[19] B. Holt, A. Tripathu, J. R. Morgan, Designing polyhema substrates that mimic the viscoelastic response of soft tissue, J. Biomechanics 44 (2011) 1491–1498.

[20] L. V. Beloussov, The dynamic architecture of a developing organism: an interdisciplinary approach to the development of organisms. , Kluwer, Dordrecht, 1998.

[21] Y. C. Fung, Biomechanics : mechanical properties of living tissues, 2nd Edition, Springer, New York, 1993.

[22] X. Trepat, L. Deng, S. An, D. Navajas, D. Tschumperlin, W. Gerthoffer, J. Butler, J. Fredberg, Universal physical responses to stretch in the living cell, Nature 447 (3) (2007) 592–596.

[23] W. N. F. nad K Onaran, W. J. Lai, Creep and Relaxation of Nonlinear Viscoelastic Materials: With an Introduction to Linear Viscoelasticity, Dover Publications, 1989.

[24] T. Belytschko, W. K. Liu, B. Moran, Nonlinear Finite Elements for Continua and Structures, Wiley and Sons, 2000.

[25] J. G. J. Beijer, J. L. Spoormaker, Solution strategies for fem analysis with nonlinear viscoelastic polymers, Comput. Struct. 80 (14-15) (2002) 1213 – 1229. http://dx.doi.org/DOI: 10.1016/S0045-7949(02)00089-5 doi:DOI: 10.1016/S0045-7949(02)00089-5.

[26] O. C. Zienkiewicz, Computational Mechanics, Ed: J T Oden, TICOM Lecture Notes on Matehmatics, 461, Springer-Verlag, 1978, Ch. Viscoplasticity, plasticity, creep and viscoplastic flow (problems of small, large and continuing deformation).

[27] T. J. R. Hughes, R. L. Taylor, Unconditionally stable algorithms for quasistatic elasto/viscoplastic finite element analysis, Comput. Struct. 8 (1978) 169–173.

[28] J. Bonet, Large strain viscoelastic constitutive models, Int. J. Solids Struct. 38 (17) (2001) 2953–2968.

[29] M. de Buhan, P. Frey, A generalized model of non-linear viscoelasticity: numerical issues and applications, Int. J. Num. Meth. Engng. 86 (2011) 1544–1557.

[30] G. A. Holzapfel, Nonlinear solid mechanics. A continuum approach for engineers, J Wiley & Sons Ltd., 2000.

[31] J. C. Simo, On a fully three-dimensional finite-strain viscoelastic damage model: Formulation and computational aspects, Comp. Meth. Appl. Mech. Engng. 60 (1987) 153–173.

[32] G. A. Holzapfel, T. C. Gasser, A viscoelastic model for fiber-reinforced composites at finite strains: continuum basis, computational aspects and applications, Comp. Meth. Appl. Mech. Engng. 190 (2001) 4379–4403.

[33] C. Tamulonis, M. Postmea, H. Q. Marlow, C. R. Magie, J. de Jong, J. Kaandorp, A cell-based model of *Nematostella vectensis* gastrulation including bottle cell formation, invagination and zippering, Dev. Biology 351 (2011) 217–228.

[34] C. J. Cyron, W. A. Wall, Consistent finite-element approach to Brownian polymer dynamics with anisotropic friction, Phys. Rev. E 82 (066705).

[35] T. Kim, W. Hwang, H. Lee, R. D. Kamm, Computational analysis of viscoelastic properties of crosslinked actin networks, PLOS Comp. Biol. 5 (7) (2009) 1–13.

[36] N. A. Cyr, R. D. Teter, Finite element elastic plastic creep analysis of two dimensional continuum with temperature dependent material properties, Comput. Struct. 3 (1973) 849–863.

[37] T. J. R. Hughes, T. K. Caughey, W. K. Liu, Finite-element methods for nonlinear elastodynamics which conserve energy, J. Appl. Mech. 45 (1978) 366–370.

[38] J. J. Muñoz, G. Jelenić, Sliding contact conditions using the master–slave approach with application on the geometracally non-linear beams, Int. J. Solids Struct. 41 (2004) 6963–6992.

[39] P. Betsch, The discrete null space method for the energy consistent integration of constrained mechanical systems. Part I: Holonomic constraints, Comp. Meth. Appl. Mech. Engng. 194 (2005) 5159–5190.

[40] O. Chaudhuri, S. Parekh, D. Fletcher, Reversible stress softening of actin networks, Nature 445 (2007) 295–298.

[41] Manfred Hahn a, Thomas Wallmersperger b, Bernd-H. Krplin. Discrete element representation of continua: Proof of concept and determination of the material parameters. Computational Materials Science 50 (2010) 391402.

Campus de Bellaterra, Edifici C
08193 Bellaterra, Spain
Tel.: +34 93 581 10 81
Fax: +34 93 581 22 02
crm@crm.cat
www.crm.cat